Structural and electronic transitions in few layers of isotopically pure hexagonal boron nitride

Jihene Zribi,[1] Lama Khalil,[1] José Avila,[2] Julien Chaste,[1] Hugo Henck,[1] Fabrice Oehler,[1] Bernard Gil,[3] Song Liu,[4] James H. Edgar,[5] Christine Giorgetti,[6] Yannick J. Dappe,[7] Emmanuel Lhuillier,[8] Guillaume Cassabois,[3] Abdelkarim Ouerghi,[1,*] and Debora Pierucci[9]

[1]*Université Paris-Saclay, CNRS, Centre de Nanosciences et de Nanotechnologies, 91120, Palaiseau, France*
[2]*Synchrotron SOLEIL and Université Paris-Saclay, L'Orme des Merisiers, BP48, 91190 Saint-Aubin, France*
[3]*Laboratoire Charles Coulomb (L2C), Université de Montpellier, CNRS, 34095 Montpellier, France*
[4]*Department of Mechanical Engineering, Columbia University, New York, NY 10027, USA*
[5]*Tim Taylor Department of Chemical Engineering, Kansas State University, Manhattan, Kansas 66506, USA*
[6]*Laboratoire des Solides Irradiés, CNRS, Ecole Polytechnique, CEA/DRF/IRAMIS, Institut Polytechnique de Paris, F-91128 Palaiseau*
[7]*SPEC, CEA, CNRS, Université Paris-Saclay, CEA Saclay, 91191 Gif-sur-Yvette Cedex, France*
[8]*Sorbonne Université, CNRS, Institut des NanoSciences de Paris, INSP, F-75005 Paris, France*
[9]*CELLS - ALBA Synchrotron Radiation Facility, Carrer de la Llum 2-26, 08290 Cerdanyola del Valles, Barcelona, Spain*

(Received 24 March 2020; revised 17 July 2020; accepted 12 August 2020; published 21 September 2020)

Hexagonal boron nitride (hBN) is attracting tremendous interest as an essential component in van der Waals heterostructures due to its ability to provide weakly interacting interfaces and because of its large bandgap. Although most of theoretical calculations yield the standard AA' stacking for few-layer hBN, the exact determination of its structural and electronic properties remains unrevealed to date. Here, we provide the direct observation of structural and electronic transitions in few layers of isotopically pure exfoliated $h^{11}BN$ flakes. Our nanoscopic angle-resolved photoemission spectroscopy measurements combined with density-functional theory calculations indicate that the stacking and the band structure can be strongly affected by the thickness of $h^{11}BN$. Hence, we show that hBN presents an AA' stacking in its bulk form and another more exotic stacking for three and four layers. Our findings open perspectives in understanding and controlling the stackings in hBN, which could be of great interest for optoelectronic applications.

DOI: 10.1103/PhysRevB.102.115141

I. INTRODUCTION

Layered two-dimensional (2D) materials are characterized by a strong anisotropy in the bonding energies along the crystal lattice directions. In-plane, the intralayer bonding is mainly of the covalent type, while out-of-plane weak interlayer interactions dominate, usually with an overwhelming van der Waals [1] character. Most of the 2D compounds such as transition-metal dichalcogenides [2,3] or hexagonal boron nitride (hBN) [4] can exist either in the bulk or in the layer form. The layer form is often obtained from the bulk through simple mechanical exfoliation [5] upon breaking the weak interlayer bonding.

Similarly to their three-dimensional counterparts, 2D materials commonly present defects that may significantly affect their physical properties. The most common type of point defect in bulk and few-layer hBN is the natural isotope variation of boron (20 at. % ^{10}B and 80 at. % ^{11}B), which has provoked a particular interest in isotopically purified hBN [6–9]. Regardless of the presence of isotopic disorder, some physical properties remain relatively unchanged: for instance, natural hBN as well as pure $h^{10}BN$ and $h^{11}BN$ all possess a wide band gap [10], low dielectric constant [11], high mechanical strength [12,13], and deep ultraviolet emission [14]. However, compared to natural hBN, pure isotopic $h^{10}BN$ and $h^{11}BN$ show a much improved thermal conductivity (an increase of 40%) and a polariton lifetime an order of magnitude higher than natural hBN [6–8].

In addition to point defects, the weak out-of-plane bonding of 2D materials facilitates the formation of disorder in the crystal structure. Various rotational and translational shifts may occur between the layers and affect the overall material properties [15–17]. An example is the well-known Bernal stacking (ABA) in graphene that can transform into a rhombohedral (ABC) stacking with significant consequences on the electronic band structure [18,19]. Structurally, hBN resembles graphite [20], with a 2D honeycomb structure relying on hexagonally organized sp^2-bonded boron and nitrogen atoms. However, as hBN possesses two types of atoms, other types of vertical stacking can occur (see Fig. 1). Although AA is the simplest stacking [Fig. 1(a)], where atoms of the same type are superimposed (B on top of B and N on top of N), it constitutes a high-energy stacking, and hence is energetically unstable. In contrast to AA, AA' [Fig. 1(b)], where B and N atoms alternate along the stacking axis (B on top of N and vice versa), is a stable stacking. Another stable stacking, although less common, is AB [Fig. 1(c)], obtained from AA by translating every other layer by a single bond length. In this stacking, half of the B atoms is superimposed with half

*abdelkarim.ouerghi@c2n.upsaclay.fr

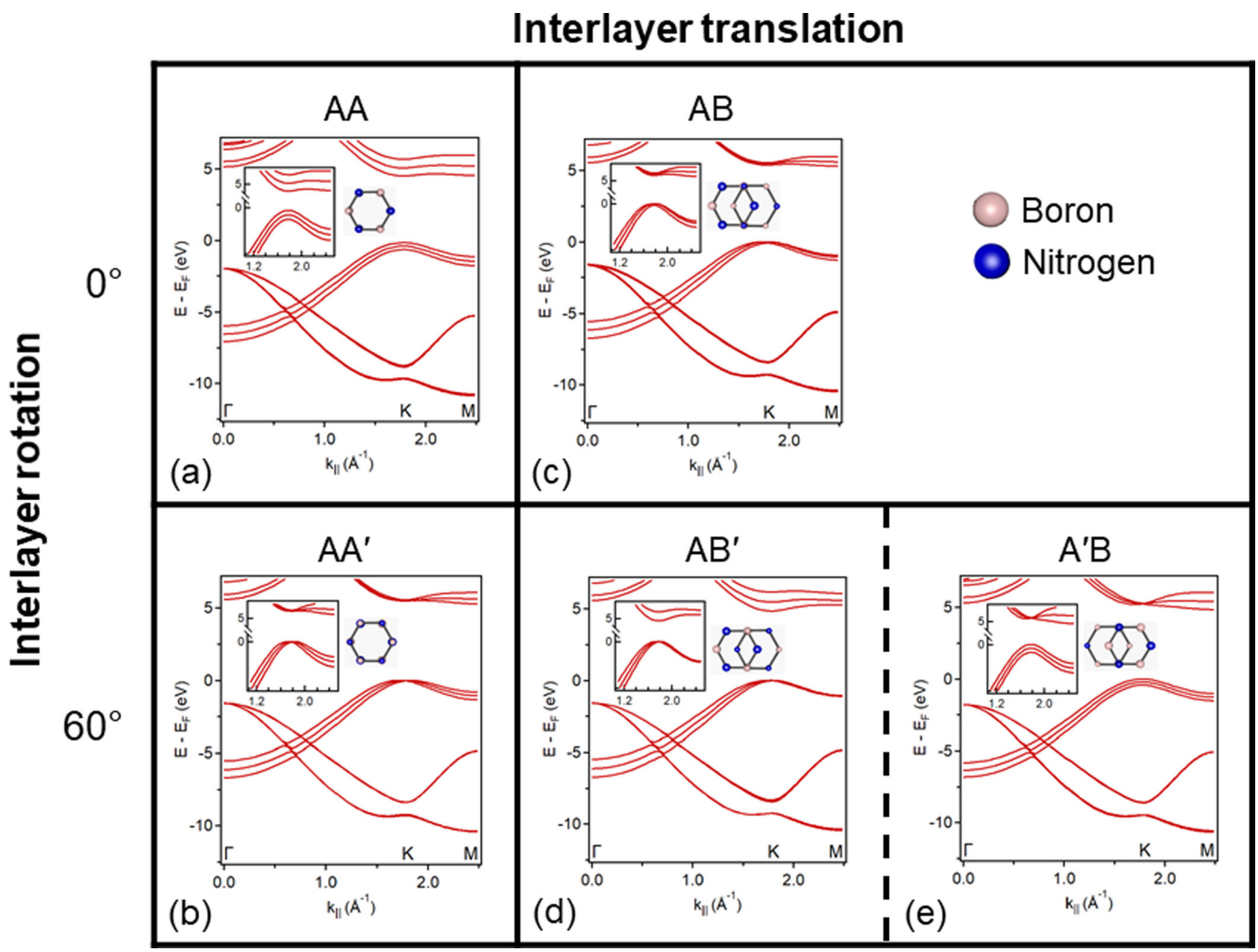

FIG. 1. Top view representation of the five possible high-symmetry stackings of hBN together with their three-layer calculated band structures. The insets display a zoomed-in version of each dispersion near the top (bottom) part of the valence (conduction) band around the *K* point. Different stackings are obtained by interlayer translation (*AB*), rotation (*AA*′) or both (*AB*′ and *A*′*B*) from the *AA* stacking, where atoms of the same type are superimposed (B on B and N on N). The drawn stackings are limited to a two-layer motif, which repeats to form the complete polytype variation. In the case of an odd number of layers, the structure is truncated to the appropriate number of layers. For the sake of clarity, the atoms in the top layer are drawn smaller than those in the bottom layer. The atoms of boron and nitrogen are represented in pink and blue colors, respectively.

of the N atoms, and the other half is located at the centers of the hexagons in the neighboring layers. By combining layer rotation and translation, we generate the *AB*′ and the *A*′*B* stackings [Figs. 1(d) and 1(e)]. In the *AB*′ (*A*′*B*) stacking, the B (N) atoms are superimposed on the two layers, and the N (B) atoms are located at the center of the hexagons.

Among the five high-symmetry stackings predicted for hBN [21–24], most of the synthesis techniques report the growth of *AA*′ [25–29]. Recently, several experimental studies have demonstrated that few-layer hBN can adopt other stackings such as Bernal stacking, *AB* [16,27,30–32]. In parallel to the experimental investigations, various theoretical studies using local-density approximation and generalized-gradient approximation calculations have anticipated that the *AA*′ and *AB* stackings are equally stable, both for the bulk and bilayer structures [33–35]. Consequently, the origin of the various stackings of hBN remains mostly unclear, despite the large amount of literature devoted to this material.

In this context, the direct visualization of the electronic band structure and its correlation with the stacking of few-layer hBN via angle-resolved photoemission spectroscopy (ARPES) is very interesting. Nevertheless, in absence of large-scale samples, it is not possible to separate contributions from areas with different stackings or/and number of layers. To overcome this issue, we use here nano-ARPES coupled with density-functional theory (DFT) calculations to restrict the analysis to nanometric-sized regions [36,18] of well-controlled thicknesses, namely, ten, four, and three layers of monoisotopic high-quality $h^{11}BN$ crystals. Thanks to the experimental energy and momentum resolution and to the calculated band structure, our results show that the stacking is strongly correlated to the layer thickness and directly affects the electronic properties of the system. In particular, our findings reveal that $h^{11}BN$ favors the *AA*′ stacking for ten layers, but another stacking is preferred when the number of layers is reduced to three or four layers.

TABLE I. Computed total energies of the five high-symmetry stackings of bulk, four-, and three-layer hBN. Δ corresponds to the change of interlayer interaction energy relative to the ground state per pair of interacting layers (equivalent to "per one layer" for bulk).

	AA	*AA′*	*AB*	*AB′*	*A′B*
	$a = 2.51$ Å $c = 7.24$ Å	$a = 2.51$ Å $c = 7.18$ Å	$a = 2.51$ Å $c = 7.17$ Å	$a = 2.51$ Å $c = 7.10$ Å	$a = 2.51$ Å $c = 7.45$ Å
Bulk					
(eV/cell)	−730.048	−730.080	−730.079	−730.072	−730.054
4 layers					
(eV/cell)	−1460.046	−1460.111	−1460.110	−1460.081	−1460.055
(eV/one layer)	−365.011	−365.028	−365.028	−365.020	−365.014
(eV/two layers)	−730.023	−730.055	−730.055	−730.041	−730.028
Δ (meV/two layers)	25	24	24	31	26
Three layers					
(eV/cell)	−1095.023	−1095.059	−1095.058	−1095.046	−1095.029
(eV/one layer)	−365.008	−365.020	−365.019	−365.015	−365.010
(eV/two layers)	−730.015	−730.040	−730.039	−730.031	−730.020
Δ (meV/two layers)	32	40	40	41	34

II. METHODS

Mechanical exfoliation of the transferred monoisotopic $h^{11}BN$ flakes on the graphene substrate was carried out using the standard Scotch tape technique.

The μ-Raman measurements were conducted at room temperature, using a commercial confocal Renishaw micro-Raman microscope with a 100× objective and a 532-nm laser excitation. The laser beam was focused onto a small spot having a diameter of ∼1 μm on the sample and its incident power was about 5 mW.

The atomic force microscopy (AFM) measurements were performed on a Veeco AFM. The nano-ARPES experiments were performed at the ANTARES beamline of the SOLEIL synchrotron light source (Saint-Aubin, France) [37]. The nano-ARPES data were taken at a photon energy of 100 eV, using linearly polarized light. All measurements were carried out at a pressure of 5×10^{-11} mbar and a temperature of 70 K. The incident photon beam is focused down to an ∼600-nm spot size on the sample surface.

Cell optimization, total energy, and band structure have been calculated within the *ab initio* framework of density-functional theory using the ABINIT code [38]. We used the Perdew-Burke-Ernzerhof generalized gradient approximation for the exchange and correlation energy [39] and optimized norm-conserving Vanderbild pseudopotential [40]. Each boron atom participates with 3 valence electrons ($2s^2\,2p^1$) and each nitrogen atom with 5 ($2s^2\,2p^3$). The van der Waals (vdW) interactions have been accounted within the vdW-DFT-D3 scheme proposed by Grimme *et al.* [41]. The vdW-DFT-D3 approach is actually among the best for the study of hBN [42]. The full optimization of the unit cell was done on the bulk counterpart of each compound. The values of the in-plane (a) and perpendicular to the plane (c) lengths of the unit cell after optimization are summarized in the first line of the table [38]. Using these cell parameters, a stacking of three layers and four layers of each compound have been built and introduced into a large supercell to mimic an isolated slab. In fact, the value of c results from the relaxation of the bulk counterpart. For the three-layer (four-layer) systems: three (four) planes are located at the distance of the interlayer distance in the relaxed bulk counterpart. This three (four) times interlayer distance is considered as the thickness of matter. The supercell height is then obtained by multiplying the thickness of matter by a factor of 3. From our experiment, the total energy is independent of the height of the supercell, as soon as it is large enough to isolate the replicas at the level of DFT calculations. In the case of the three-layer systems, the vacuum between the replicas is around 21 Å, and for the four-layer systems, it is around 29 Å. These values are thus large enough to isolate replicas in our calculations. The density has been computed using a Monkhorst-Pack grid of $(11\times11\times2)$ k points, with an energy cutoff of 870.76 eV. The band structures have been sampled with 41 points along ΓK and ΓM. The total energies are reported in Table I for bulk, three layers, and four layers for the five stackings. Energies are referenced to the *AA′* stacking, and are in meV per unit cell (two B and two N atoms).

III. RESULTS AND DISCUSSION

In addition to the atomic structure, Fig. 1 also shows the calculated electronic band structure for each polytype. As the latter strongly depends on the number of layers, we only consider a three-layer structure for all DFT calculations of Fig. 1. Although the overall dispersion looks nearly similar, there are differences between all polytypes for all occupied and unoccupied bands, especially for the top of the valence band near the K point (see also Fig. S1 [43] for the calculated band structure of bulk hBN). For instance, the π bands are degenerate for *AA′*, AB and *AB′*, whereas they split into 3 parabolic branches for AA and *A′B*. On the other hand, the 3-layer structures of AA and *A′B* present an overall similar band dispersion. However, by superimposing the calculated bands of the two stackings (Supplemental Material, Fig. S2 [43]), we notice that the largest difference is for the σ bands located at higher binding energies along the KM high-symmetry

direction. Additionally, the magnitude of the π-band energy splitting at the K point is different for both stackings. We can also remark that $A'B$ have an indirect band gap, whereas AA presents a direct band gap. Therefore, it is possible to precisely fingerprint each polytype based on the specifics of its band dispersion.

We also calculated the total cohesive energies for three layers, four layers, and for the bulk crystal in the five possible different stackings presented in Fig. 1. Quantitatively, the computed energy values are summarized in Table I. As above-mentioned, the AA' stacking, where the hexagons are superimposed with an alternation of B and N atoms in each column, is considered to be the natural stacking of hBN. Our results show that it is indeed the stacking which presents the lowest total energy for the bulk, as well as for three and four layers. In the AB stacking, the atoms can be either in the middle of the hexagons, and thus without neighbors in the adjacent layers, or piled up in columns with an alternation of B and N atoms. The fact that some columns are "missing" has consequences on the relaxed geometry, which presents a slightly smaller c length with respect to AA'. However, due to the alternate piling in the remaining columns, the stacking is equally stable to AA', regardless of the number of layers. When the columns are only made of N atoms (the case of $A'B$), the c length presents the highest numerical value (7.45 Å), whereas when they consist only of B atoms (the AB' case), the c length becomes the smallest (7.10 Å). For the AA stacking, where both kinds of columns made of either N or B atoms are present, the cell length c has a value in-between the ones of $A'B$ and AB' (7.24 Å). Concerning the total energy, the latter three stackings (namely, AA, $A'B$, and AB') are less stable than the AA' and AB ones. Similar calculations for the total cohesive energy have been previously conducted for bulk hBN. They, however, yield some discrepancies with respect to our data [21,22,34,35]; this is due to the fact that the results are extremely sensitive to the computational details and approaches [42,44]. On the other hand, the stacking hierarchy from the lowest to the highest energy in this work is in agreement with some studies from literature [34,35], but inconsistent with others [21,22]. Experimentally, the determination of the stackings of few layers hBN remains mostly unclear. In this respect, the direct visualization of the electronic band structure and its correlation with the stacking of few-layer hBN via ARPES is very interesting. Charging effects are a common issue in photoemission studies for insulating materials, such as hBN. However, they can be eliminated by thinning the material via exfoliation and by using the appropriate substrate [45]. In our previous study, we proved that it is possible to resolve the π bands of exfoliated hBN transferred on an epitaxial graphene underlayer [46]. For that, we use in this study exfoliated monoisotopic $h^{11}BN$ crystals transferred onto single-layer graphene/SiC(0001).

To quickly assess the crystalline and chemical purity of our sample, we used micro-Raman (μ-Raman) spectroscopy. Figure 2(a) compares the μ-Raman spectrum obtained from our monoisotopic $h^{11}BN$ crystal with spectra from other natural $h^{Na}BN$ and monoisotopic $h^{10}BN$ samples. Only the high-energy active mode E_{2g} is visible in the wave-number range between 1340 and 1420 cm^{-1}. This mode corresponds to the stretching of the B–N bond within the hexagonal BN basal plane [7]. The energy of this E_{2g} phonon is 1356, 1365, and 1393 cm^{-1} for $h^{11}BN$, $h^{Na}BN$, and $h^{10}BN$, respectively. Note that the $h^{Na}BN$ peak is positioned between the peaks of $h^{10}BN$ and $h^{11}BN$, since it is an isotopic mixture of both. The Raman linewidths are significantly narrower for monoisotopic $h^{10}BN$ ($3.8 \pm 0.1\ cm^{-1}$) and monoisotopic $h^{11}BN$ ($3.9 \pm 0.1\ cm^{-1}$) than for the naturally abundant hBN sample ($8.1 \pm 0.1\ cm^{-1}$), in agreement with previous studies [6–8,47]. The small linewidth values for monoisotopic hBN crystals reflect the high crystalline quality of these samples and indicate the absence of phonon scattering due to isotopic mass disorder [23].

Further information on the properties of our sample can be obtained by investigating a region of interest by different techniques: optical microscopy, AFM, and nano-ARPES. Optically, the transferred $h^{11}BN$ flake with different thicknesses, marked with a white line, presents a slight contrast with respect to the underlying graphene/SiC substrate, as shown in Fig. 2(b). In the corresponding AFM image to Fig. 2(b) [see Fig. 2(c)], we can also identify the same flake (delimited by a white contour) on the stepped graphene/SiC surface. The thicknesses in the hBN region are assessed to ten, four, and three layers, as measured by AFM (see Supplemental Material, Fig. S3 [43]). In particular, the ten-layer area allows one to measure the bulklike characteristics of $h^{11}BN$. In Fig. 2(d), we present the spatially resolved photoelectron intensity map for the same region on the sample, taken at a photon energy of 100 eV and integrated around the valence-band maximum (VBM) along the ΓKM high-symmetry direction. Based on our nano-ARPES measurements, we found that the $h^{11}BN$ Brillouin zone (BZ) is rotated by 39° with respect to the graphene BZ (see Fig. S4 [43]). This arbitrary twist angle simply stems from the transfer process of the $h^{11}BN$ flakes, which is performed without any rotational control. The nano-ARPES map in Fig. 2(d) reveals the presence of various microscopic domains within the hBN flake. According to the AFM image, the area marked as ten layers in the ARPES map, where the intensity color scale is green, corresponds to the bulklike region, while the other areas with lower intensity (blue color) are relative to three and four layers.

Next, we present in Figs. 3(a)–3(c) the valence-band structures along the ΓKM direction, obtained by nano-ARPES from three distinct point measurements on the ten-, four-, and three-layer regions of Fig. 2(d), respectively. The sharpness of the different bands can be attributed to the high quality of the $h^{11}BN$ samples. The π and σ bands of hBN can be easily identified in all maps for all thicknesses. On one hand, the π states disperse from the Γ point up towards the VBM located at the K point in the ΓK direction, then down to the M point in the KM direction. On the other hand, the σ bands, degenerate at the Γ point, disperse downwards to the K point. We notice from the spectra in Fig. 3 that the VBM downshifts from 2.94 eV binding energy (BE) for ten layers to 3.2 eV BE for the three-layer domain. This VBM shift of the π bands of 0.26 eV when decreasing the thickness of hBN can be attributed to an interfacial electron transfer from the n-doped bilayer graphene to hBN. Actually, the charge transfer reduces the excess positive charge of hBN, similarly to what is reported for GaSe/graphene heterostructures [48]. Since it only occurs at the interface, the reduction of the excess

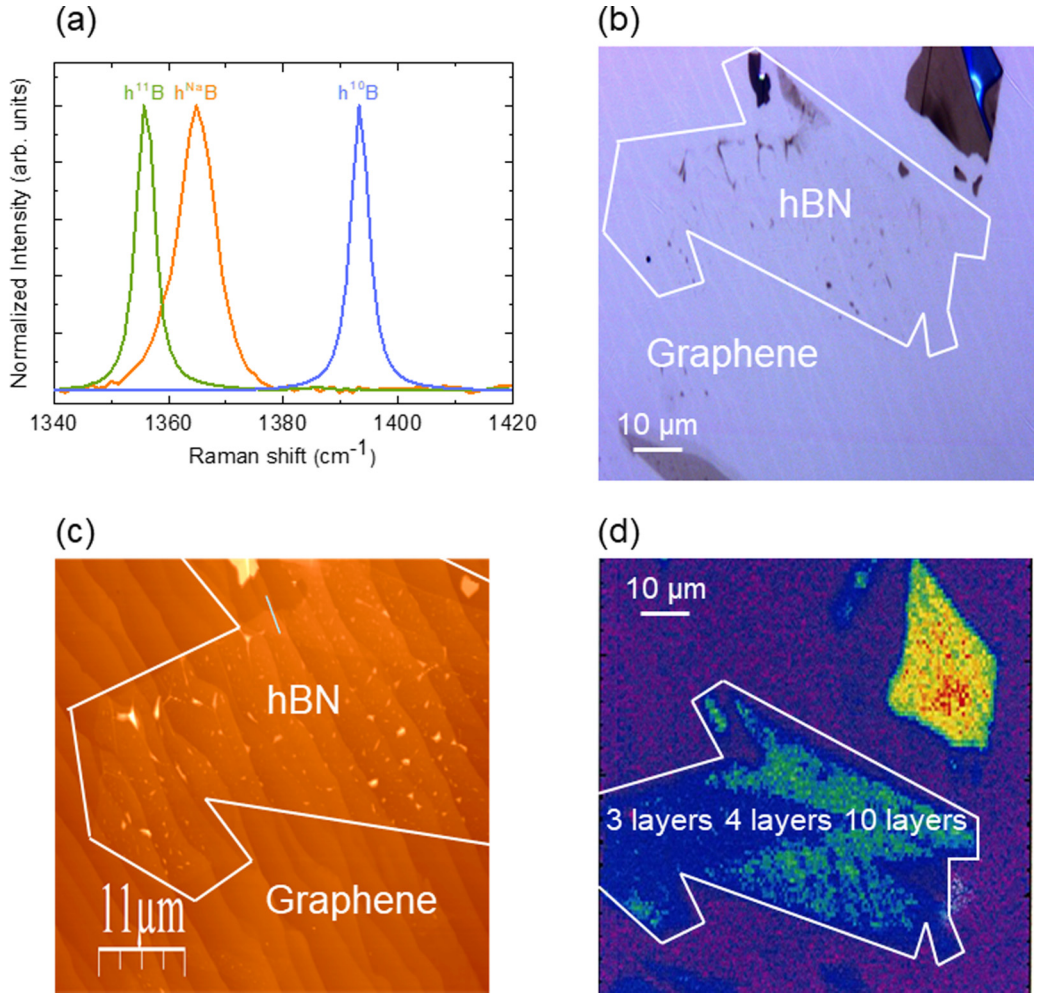

FIG. 2. Structural and electronic properties of the exfoliated $h^{11}BN$ crystal. (a) μ-Raman spectra acquired at room temperature from three different hBN samples, namely, the monoisotopic $h^{10}BN$ and $h^{11}BN$ crystals and the standard $h^{Na}BN$ specimen. (b) Typical optical image, in which the $h^{11}BN$ domains exhibit a slightly different contrast with respect to the graphene substrate. (c) AFM image of the region delimited by a white contour in (b). (d) A spatially resolved intensity map, integrated around the VBM along the ΓKM high-symmetry direction, around the region delimited by a white line in the optical image of (b).

positive charge is more pronounced for three and four layers than for bulk hBN.

In order to ascribe each electronic band structure of Figs. 3(a)–3(c) to its corresponding crystallographic stacking, we compared our experimental ARPES data with the band-structure calculations in the DFT framework for freestanding hBN layers [see Figs. 3(d)–3(f)]. The DFT calculated bands are shifted to account for the Fermi-level position, and expanded by 17% in energy to match the experimental total bandwidth [49–51]. This scaling effectively incorporates many-body interactions not included in the calculations. The matching procedure is found to produce marginal changes in the position and splitting of the calculated π bands around the top part of the valence band, but rather affects the band dispersion at higher binding energies. The main features are well reproduced by the calculated band structures along all high-symmetry directions for all ARPES spectra. The measured and DFT calculated band structures agree for bulklike hBN [Fig. 3(d)] with the AA' stacking. This supports that the most stable stacking for bulk hBN is AA', consistent with previous experimental studies and theoretical predictions [46]. Moving to Figs. 3(e) and 3(f), we remark that the nano-ARPES data likely agree with the DFT calculations for the $A'B$ stacking (this will be further discussed below), specifically for the σ bands along the KM high-symmetry direction (see Fig. S2 [43]). Therefore, the nano-ARPES maps clearly reveal that the band structure and the stacking differ according to the layer thickness.

The difference in the dispersion between the photoelectron intensity maps of Figs. 3(a)–3(c) around the K point [see Figs. 4(a)–4(c)] are compared with the DFT calculations [Figs. 4(d)–4(f)]. The π bands are degenerate for the ten-layer region, whereas they split into three and four parabolic branches for the three- and four-layer domains, respectively (see insets showing the second derivative on which the theory is overplotted). This difference in the electronic band structure, i.e., the π-band degeneracy lifting for three and four layers with respect to ten layers, mainly comes from a modification in the stacking. Note that we explored the band dispersion of several points on the flake (via a line scan), and we constantly obtained the same dispersion for each thickness. We also explored the electronic structure of the sibling $h^{10}BN$

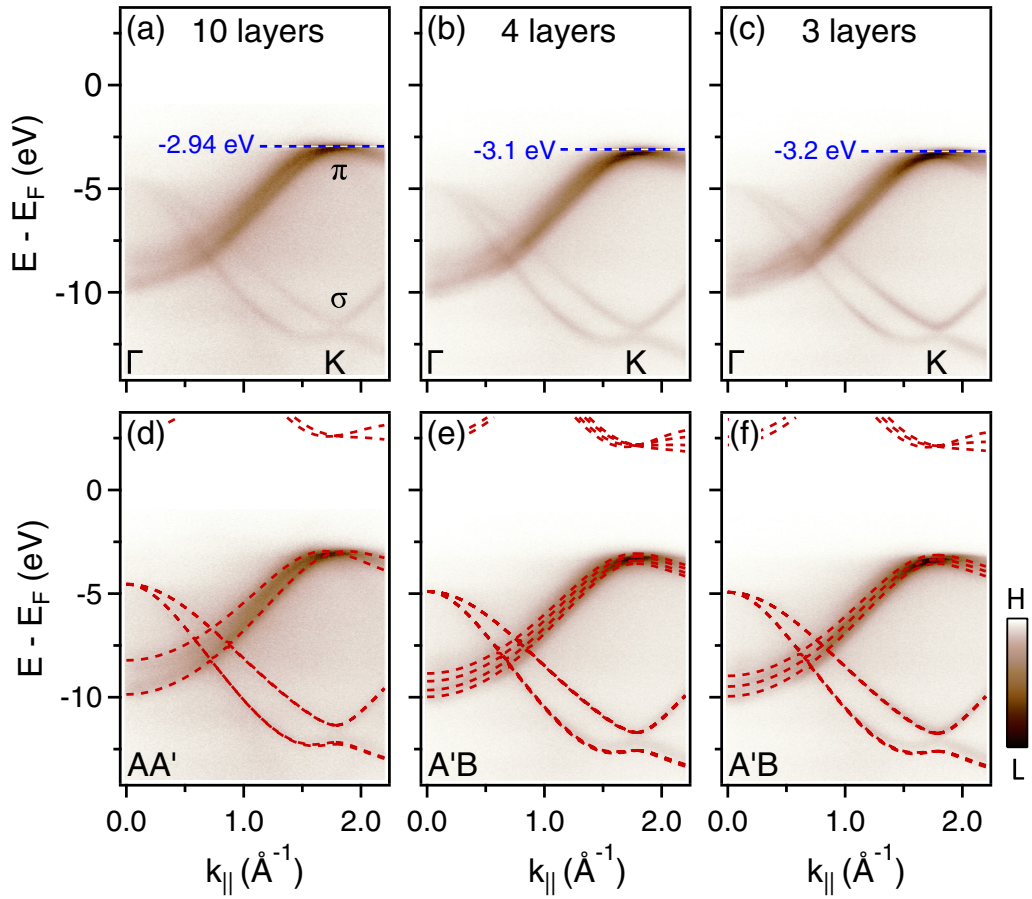

FIG. 3. Structural and electronic transitions in few-layers of $h^{11}BN$. (a)–(c) High-resolution nano-ARPES measurements along the ΓKM direction, acquired with an incident photon energy of 100 eV, for ten-, four-, and three-layer hBN, respectively. A charge transfer from the n-doped bilayer graphene to $h^{11}BN$ takes place, thereby reducing the excess positive charge of $h^{11}BN$. (d)–(f) Theory versus experiment. Comparison of the photoelectron intensity maps of (a)–(c) with DFT calculations. The nano-ARPES intensity maps reveal that the band structure varies according to the layer thickness.

compound for four layers along the ΓKM direction, and no relevant difference was found in its dispersion with respect to the four-layer $h^{11}BN$ one (see Fig. S5 [43]). The second derivative of bulk hBN [inset of Fig. 4(d)] matches the calculations well for the AA' stacking, whereas the ones of three and four layers may agree either with $A'B$ [insets of Figs. 4(e) and 4(f)] or with AA [insets of Figs. 4(h) and 4(i)].

This begs the question: does the measured structure for the three- and four-layer spots correspond to AA or to $A'B$? Since the energies predicted by our calculations are quite similar for the two stackings for three and four layers (see Table I), we first compared our nano-ARPES data at higher binding energies with the DFT calculations of both stackings. As above-mentioned, we find that the dispersion better agrees with the calculated bands of $A'B$, specifically for the σ bands along the KM high-symmetry direction. Secondly, we compared for the two stackings the energy splitting of the π bands, δ, between the upper and the lower branches [see inset of Fig. 4(f)]. Quantitatively, the value of the energy splitting is of 0.34 eV for the three-layer measured spectrum, whereas it is of 0.4 and 0.48 eV for the calculated bands of $A'B$ and AA, respectively. This suggests that the calculated band dispersion around K for $A'B$ is in slightly better agreement with the experiment than the one for AA. This can also be better visualized by comparing the energy distribution curve (EDC), obtained by integrating the intensity map in a wave-vector window of $0.05\,\text{Å}^{-1}$ around $k = 1.78\,\text{Å}^{-1}$, with the positions of the calculated bands of AA and $A'B$ [see Fig. 4(g)]. In particular, the lowest π band at higher binding energies for AA does not match the measured dispersion well.

Therefore, based on Figs. 4 and S2 [43], we conclude that the overall calculated dispersion of $A'B$ for both σ and π bands is in better agreement with the experimental data than the one of AA. According to our calculations, three or four layers of hBN with the AA ($A'B$) stacking present a direct (indirect) band gap. Consequently, to further confirm the obtainment of the $A'B$ for three and four layers, one should measure the optical band gap with microphotoluminescence in order to verify its indirect nature. A second possibility is to investigate the unoccupied electronic band structure by means of inverse photoemission spectroscopy or by time-resolved ARPES.

The small total-energy difference of 6 meV/cell between $A'B$ and AA for three layers indicates that the stacking formation mainly depends on the experimental growth of hBN and/or on the interaction between hBN and the substrate. Additional experiments and calculations are thus required to further understand the impact of the substrate on the stacking

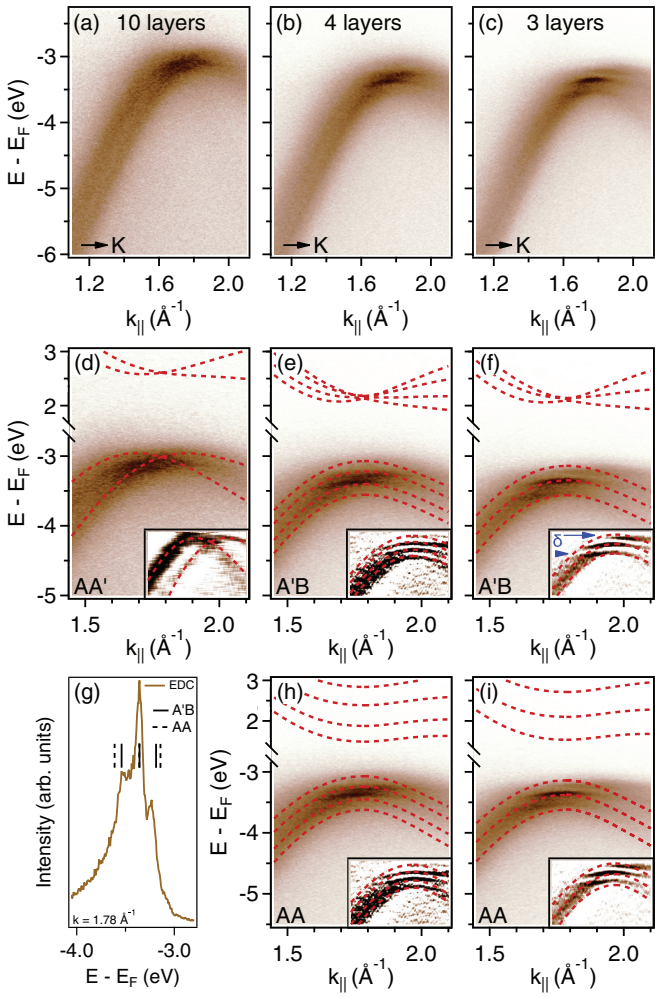

FIG. 4. Nano-ARPES study around the K point. (a)–(c) Difference in the dispersion between the ARPES spectra of Figs. 3(a)–3(c) around the K point for ten-, four-, and three-layer hBN, respectively. (d)–(f) Comparison between the experimental data and DFT calculations corresponding to AA' for bulk and $A'B$ for three and four layers. Insets display the second derivatives of the photoelectron intensity maps on which the theory is overplotted. (g) EDC obtained by integrating the nano-ARPES map in (c). The black plain and dashed lines indicate the positions of the calculated $A'B$ and AA bands, respectively. (h), (i) Comparison between the experimental data and DFT calculations for the AA stacking. Insets of (h) and (i) show calculations for AA superimposed on the second derivative images. The DFT calculations for the $A'B$ and AA stackings are scaled by 17% to match the overall bandwidth of the experiment.

of these ultrathin samples, and to determine the layer thickness at which the structural transition between ten and four layers occurs. From our calculations, we found that the stackings are intimately related to the interaction potential between the hBN layers through their respective atomic alignments, which can strongly affect the interlayer distance. Therefore, the resulting interaction due to different atomic arrangements represents the key parameter that induces the modification in the stacking of hBN. Our findings on the electronic and structural transitions in few-layer hBN are of utmost interest for applications, specifically in tunneling devices made by few-layer hBN sandwiched between two layers of graphene or two layers of 2D materials. Most previous studies have focused on the use of the AA' stacking for barrier tunneling experiments, but our results show that another stacking is preferred when the number of layers is decreased to three or four layers. This indicates that further efforts, taking into account all the above-mentioned results, are required to understand more in detail the effect of the stackings in applications, for instance, in tunneling or electronic devices.

IV. CONCLUSION

In summary, we have successfully conducted high-resolution nano-ARPES experiments on high-quality exfoliated monoisotopic $h^{11}BN$ crystals. Our experimental results coupled with theoretical calculations show that the stacking for bulk $h^{11}BN$ is AA', whereas it is most likely $A'B$ for three and four layers. The dispersion of the π bands is changed according to the stacking, specifically at the K point. In particular, for bulk hBN, the π bands are degenerate at the K point, whereas for few-layer hBN, the degeneracy is lifted and these states reveal a splitting in energy. Remarkably, our findings show that interaction due to the different atomic arrangements between the hBN layers is the key parameter that affects the stacking, the interlayer distance, and the electronic structure. Finally, by taking into account the spot size of the nano-ARPES beam, we argue that we have obtained large domains presenting the exotic $A'B$ stacking for three and four layers, which could be of great importance for future applications.

The authors declare no competing financial interest.

ACKNOWLEDGMENTS

We acknowledge the financial support by RhomboG (Grant No. ANR-17-CE24-0030), MagicValley (Grant No. ANR-18-CE24-0007), and Graskop (Grant No. ANR-19-CE09-0026). We also thank the support ERC starting grant blackQD (Grant No. 756225).This work is supported by a public grant overseen by the French National Research Agency (ANR) as part of the "Investissements d'Avenir" program (Labex NanoSaclay, Reference No. ANR-10-LABX-0035). Support from the Materials Engineering and Processing program of the National Science Foundation, Award No. CMMI 1538127 is greatly appreciated. Computer time has been granted by GENCI (Project No. 544) and by CEA/DRF.

[1] K. S. Novoselov, A. Mishchenko, A. Carvalho, and A. H. Castro Neto, Science **353**, aac9439 (2016).

[2] R. Cheng, S. Jiang, Y. Chen, Y. Liu, N. Weiss, H.-C. Cheng, H. Wu, Y. Huang, and X. Duan, Nat. Commun. **5**, 5143 (2014).

[3] R. Cheng, D. Li, H. Zhou, C. Wang, A. Yin, S. Jiang, Y. Liu, Y. Chen, Y. Huang, and X. Duan, Nano Lett. **14**, 5590 (2014).

[4] G. Cassabois, P. Valvin, and B. Gil, Nat. Photon. **10**, 262 (2016).

[5] K. S. Novoselov, A. K. Geim, S. V. Morozov, D. Jiang, Y. Zhang, S. V. Dubonos, I. V. Grigorieva, and A. A. Firsov, Science **306**, 666 (2004).

[6] A. J. Giles, S. Dai, I. Vurgaftman, T. Hoffman, S. Liu, L. Lindsay, C. T. Ellis, N. Assefa, I. Chatzakis, T. L. Reinecke, J. G. Tischler, M. M. Fogler, J. H. Edgar, D. N. Basov, and J. D. Caldwell, Nat. Mater. **17**, 134 (2018).

[7] T. Q. P. Vuong, S. Liu, A. Van der Lee, R. Cuscó, L. Artús, T. Michel, P. Valvin, J. H. Edgar, G. Cassabois, and B. Gil, Nat. Mater. **17**, 152 (2018).

[8] C. Yuan, J. Li, L. Lindsay, D. Cherns, J. W. Pomeroy, S. Liu, J. H. Edgar, and M. Kuball, Commun. Phys. **2**, 43 (2019).

[9] R. Cuscó, L. Artús, J. H. Edgar, S. Liu, G. Cassabois, and B. Gil, Phys. Rev. B **97**, 155435 (2018).

[10] Y. Kubota, K. Watanabe, O. Tsuda, and T. Taniguchi, Science **317**, 932 (2007).

[11] H. Yang, H. Fang, H. Yu, Y. Chen, L. Wang, W. Jiang, Y. Wu, and J. Li, Nat. Commun. **10**, 854 (2019).

[12] C. Zhi, Y. Bando, C. Tang, H. Kuwahara, and D. Golberg, Adv. Mater. **21**, 2889 (2009).

[13] K. K. Kim, A. Hsu, X. Jia, S. M. Kim, Y. Shi, M. Hofmann, D. Nezich, J. F. Rodriguez-Nieva, M. Dresselhaus, T. Palacios, and J. Kong, Nano Lett. **12**, 161 (2012).

[14] T. Q. P. Vuong, G. Cassabois, P. Valvin, E. Rousseau, A. Summerfield, C. J. Mellor, Y. Cho, T. S. Cheng, J. D. Albar, L. Eaves, C. T. Foxon, P. H. Beton, S. V. Novikov, and B. Gil, 2D Mater. **4**, 021023 (2017).

[15] R. Ribeiro-Palau, C. Zhang, K. Watanabe, T. Taniguchi, J. Hone, and C. R. Dean, Science **361**, 690 (2018).

[16] C.-J. Kim, L. Brown, M. W. Graham, R. Hovden, R. W. Havener, P. L. McEuen, D. A. Muller, and J. Park, Nano Lett. **13**, 5660 (2013).

[17] Y. Cao, V. Fatemi, S. Fang, K. Watanabe, T. Taniguchi, E. Kaxiras, and P. Jarillo-Herrero, Nature (London) **556**, 43 (2018).

[18] H. Henck, J. Avila, Z. Ben Aziza, D. Pierucci, J. Baima, B. Pamuk, J. Chaste, D. Utt, M. Bartos, K. Nogajewski, B. A. Piot, M. Orlita, M. Potemski, M. Calandra, M. C. Asensio, F. Mauri, C. Faugeras, and A. Ouerghi, Phys. Rev. B **97**, 245421 (2018).

[19] L. Gong, R. J. Young, I. A. Kinloch, S. J. Haigh, J. H. Warner, J. A. Hinks, Z. Xu, L. Li, F. Ding, I. Riaz, R. Jalil, and K. S. Novoselov, ACS Nano **7**, 7287 (2013).

[20] D. Pacilé, J. C. Meyer, Ç. Ö. Girit, and A. Zettl, Appl. Phys. Lett. **92**, 133107 (2008).

[21] S. M. Gilbert, T. Pham, M. Dogan, S. Oh, B. Shevitski, G. Schumm, S. Liu, P. Ercius, S. Aloni, M. L. Cohen, and A. Zettl, 2D Mater. **6**, 021006 (2019).

[22] G. Constantinescu, A. Kuc, and T. Heine, Phys. Rev. Lett. **111**, 036104 (2013).

[23] H. Henck, D. Pierucci, Z. Ben Aziza, M. G. Silly, B. Gil, F. Sirotti, G. Cassabois, and A. Ouerghi, Appl. Phys. Lett. **110**, 023101 (2017).

[24] R. M. Ribeiro and N. M. R. Peres, Phys. Rev. B **83**, 235312 (2011).

[25] R. S. Pease, Nature (London) **165**, 722 (1950).

[26] S. M. Kim, A. Hsu, M. H. Park, S. H. Chae, S. J. Yun, J. S. Lee, D.-H. Cho, W. Fang, C. Lee, T. Palacios, M. Dresselhaus, K. K. Kim, Y. H. Lee, and J. Kong, Nat. Commun. **6**, 8662 (2015).

[27] J. H. Warner, M. H. Rümmeli, A. Bachmatiuk, and B. Büchner, ACS Nano **4**, 1299 (2010).

[28] N. Alem, R. Erni, C. Kisielowski, M. D. Rossell, W. Gannett, and A. Zettl, Phys. Rev. B **80**, 155425 (2009).

[29] W. J. Yu, W. M. Lau, S. P. Chan, Z. F. Liu, and Q. Q. Zheng, Phys. Rev. B **67**, 014108 (2003).

[30] A. Shmeliov, J. S. Kim, K. B. Borisenko, P. Wang, E. Okunishi, M. Shannon, A. I. Kirkland, P. D. Nellist, and V. Nicolosi, Nanoscale **5**, 2290 (2013).

[31] M. H. Khan, G. Casillas, D. R. G. Mitchell, H. K. Liu, L. Jiang, and Z. Huang, Nanoscale **8**, 15926 (2016).

[32] M. H. Khan, H. K. Liu, X. Sun, Y. Yamauchi, Y. Bando, D. Golberg, and Z. Huang, Mater. Today **20**, 611 (2017).

[33] J. L. Yin, M. L. Hu, Z. Yu, C. X. Zhang, L. Z. Sun, and J. X. Zhong, Phys. B: Condens. Matter **406**, 2293 (2011).

[34] N. Ooi, A. Rairkar, L. Lindsley, and J. B. Adams, J. Phys.: Condens. Matter **18**, 97 (2006).

[35] L. Liu, Y. P. Feng, and Z. X. Shen, Phys. Rev. B **68**, 104102 (2003).

[36] D. Pierucci, H. Henck, J. Avila, A. Balan, C. H. Naylor, G. Patriarche, Y. J. Dappe, M. G. Silly, F. Sirotti, A. T. C. Johnson, M. C. Asensio, and A. Ouerghi, Nano Lett. **16**, 4054 (2016).

[37] J. Zribi, L. Khalil, B. Zheng, J. Avila, D. Pierucci, T. Brulé, J. Chaste, E. Lhuillier, M. C. Asensio, A. Pan, and A. Ouerghi, npj 2D Mater. Appl. **3**, 27 (2019).

[38] X. Gonze, B. Amadon, P.-M. Anglade, J.-M. Beuken, F. Bottin, P. Boulanger, F. Bruneval, D. Caliste, R. Caracas, M. Côté, T. Deutsch, L. Genovese, P. Ghosez, M. Giantomassi, S. Goedecker, D. R. Hamann, P. Hermet, F. Jollet, G. Jomard, S. Leroux, M. Mancini, S. Mazevet, M. J. T. Oliveira, G. Onida, Y. Pouillon, T. Rangel, G.-M. Rignanese, D. Sangalli, R. Shaltaf, M. Torrent, M. J. Verstraete, G. Zerah, and J. W. Zwanziger, Comput. Phys. Commun. **180**, 2582 (2009).

[39] J. P. Perdew, K. Burke, and M. Ernzerhof, Phys. Rev. Lett. **77**, 3865 (1996).

[40] D. R. Hamann, Phys. Rev. B **88**, 085117 (2013).

[41] S. Grimme, J. Antony, S. Ehrlich, and H. Krieg, J. Chem. Phys. **132**, 154104 (2010).

[42] I. V. Lebedeva, A. V. Lebedev, A. M. Popov, and A. A. Knizhnik, Comput. Mater. Sci. **128**, 45 (2017).

[43] See Supplemental Material at http://link.aps.org/supplemental/10.1103/PhysRevB.102.115141 for all supplemental figures (Fig. S1: Band structure calculations for bulk hBN; Fig. S2: Comparison between the three-layer calculated band structure of *AA* and *A′B*; Fig. S3: Calibration of the thickness using a reference flake of $h^{11}BN$ by means of μ-Raman and AFM; Fig. S4: Angle between the graphene layer and $h^{11}BN$; Fig. S5: Electronic band structure of four-layer $h^{10}BN$).

[44] S. Zhou, J. Han, S. Dai, J. Sun, and D. J. Srolovitz, Phys. Rev. B **92**, 155438 (2015).

[45] R. J. Koch, J. Katoch, S. Moser, D. Schwarz, R. K. Kawakami, A. Bostwick, E. Rotenberg, C. Jozwiak, and S. Ulstrup, Phys. Rev. Mater. **2**, 074006 (2018).

[46] H. Henck, D. Pierucci, G. Fugallo, J. Avila, G. Cassabois, Y. J. Dappe, M. G. Silly, C. Chen, B. Gil, M. Gatti, F. Sottile, F. Sirotti, M. C. Asensio, and A. Ouerghi, Phys. Rev. B **95**, 085410 (2017).

[47] S. Liu, R. He, L. Xue, J. Li, B. Liu, and J. H. Edgar, Chem. Mater. **30**, 6222 (2018).

[48] Z. Ben Aziza, D. Pierucci, H. Henck, M. G. Silly, C. David, M. Yoon, F. Sirotti, K. Xiao, M. Eddrief, J.-C. Girard, and A. Ouerghi, Phys. Rev. B **96**, 035407 (2017).

[49] D. Pierucci, H. Sediri, M. Hajlaoui, J. Girard, T. Brumme, M. Calandra, E. Velez-fort, G. Patriarche, M. G. Silly, G. Ferro, V. Soulière, M. Marangolo, F. Sirotti, F. Mauri, and A. Ouerghi, ACS Nano **9**, 5432 (2015).

[50] H. Guyot, P. Achatz, A. Nicolaou, P. Le Fèvre, F. Bertran, A. Taleb-Ibrahimi, and E. Bustarret, Phys. Rev. B **92**, 045135 (2015).

[51] M. S. Hybertsen and S. G. Louie, Phys. Rev. B **34**, 5390 (1986).